MDPI

Article

Crystal Growth of Osmium(IV) Dioxide in Chlorine-Bearing Hydrothermal Fluids

Haibo Yan [1,2,3], Zhuoyu Liu [1], Jian Di [1,3,4] and Xing Ding [1,3,*]

1. State Key Laboratory of Isotope Geochemistry, Guangzhou Institute of Geochemistry, Chinese Academy of Sciences, Guangzhou 510640, China
2. CAS Key Laboratory of Mineralogy and Metallogeny, Guangzhou Institute of Geochemistry, Chinese Academy of Sciences, Guangzhou 510640, China
3. CAS Center for Excellence in Deep Earth Science, Guangzhou 510640, China
4. College of Earth and Planetary Sciences, University of Chinese Academy of Sciences, Beijing 100049, China
* Correspondence: xding@gig.ac.cn

Abstract: A mineral's morphology is usually related to its growth process and environment. This study reported crystal growth of OsO_2 through hydrolysis experiments of K_2OsCl_6 at 150–550 °C and 100 MPa to investigate the growth mechanism of OsO_2 and the transport and enrichment of Os in chlorine-bearing hydrothermal fluids. Time-series experimental results showed that the OsO_2 crystals grow from 40–150 nm irregular nanoparticles to 150–450 nm nanospheres with time. As the temperature and initial solution concentrations increase, OsO_2 can form more uniform and larger OsO_2 nanosphere crystals, suggesting a positive effect of temperature and initial solution concentration on the crystal growth of OsO_2. The results indicate that the nucleation and aggregate growth driven by the hydrolysis of Os–chloride complex controls the early growth of OsO_2 crystals for a short duration; however, after the hydrolysis reaches equilibrium, the growth process of OsO_2 nanosphere crystals is dominated mostly by the Ostwald ripening, where the diffusion of Os ions along the fluid–nanocrystal boundary facilitates the coarsening. Given that the transport and cycle of Os from the lithosphere to the hydrosphere is controlled mainly by the stability of the Os–chloride complex, OsO_2 nanosphere crystals could occur in seafloor hydrothermal vent systems.

Keywords: osmium; crystal growth; nanosphere; chlorine-bearing fluids; ostwald ripening

1. Introduction

Water–rock interactions are one of the most critical mineralization and material recycling processes on earth [1]. They can occur widely in seafloor hydrothermal vent systems, promoting metal extraction from the mantle-derived magma and wall rocks [2–6]. In such a scenario, the extracted metal elements can be transported in the hydrothermal fluids and enriched in the minerals, encrustations, and sediments, resulting in a potentially substantial resource of minerals such as Fe, Mn, Zn, Pb, Co, Cu, Ag, Sn, REEs, PGEs, etc. [7–10]. Among them, PGEs usually transport as chloride complexes in the deep sea and are then enriched in the encrustations as isomorphic compounds or metals or are scattered in the ocean floor sediments, providing substantial potential resources [11,12]. In seafloor hydrothermal systems, PGEs are usually oxidized to a high state (+2 or +4) by oxidized seafloor hydrothermal fluids and then precipitated into the ocean sediments and muds [13,14], contrasting sharply with the low state (0 and +2) PGEs which could exist during the magmatic process in the deep earth [15–17].

As a representative element of PGEs, osmium (Os) is an important functional and structural material with high ionic and magnetic conductivity as well as high temperature-resistant and corrosion-resistant properties [18]. It can be widely used in microbial reagents, radiation protection materials, catalysts, gas fixing agents, electrode conductivity materials, and other fields [19–22]. Osmium-rich crystal materials such as osmium (IV) dioxide

also have an essential role in electrochemical and electro-mechanical industries [21,23]. However, only a rutile-type OsO_2 has been synthesized using the chemical vapor transport (CVT) method and researched [18,24]. Other precipitation and nucleation properties of high-valence Os ions, as well as their crystal growth in hydrothermal fluids, are still poorly understood, which hinders future applications and a deep understanding of Os enrichment and deposition in the oxidized seafloor hydrothermal fluids.

To fill this gap, this study adopts experimental methods to probe the precipitation process of Os(IV) and its growth mechanism in chlorine-bearing hydrothermal fluids. This study could enrich our understanding of the transport and enrichment of Os in the hydrothermal vent system.

2. Materials and Methods

2.1. Materials and Instruments

The experimental materials in this study included potassium chlorosmate (K_2OsCl_6, Os $\geq$ 38.7%, AR, Macklin, Shanghai, China) and ethanol (AR, Huada, Guangzhou, China). K_2OsCl_6 has a high density of 3.470 g/cm^3 and is one of the most stable chemicals among Os–Cl complexes at room temperature and ambient pressure. It was diluted with deionized water to produce the initial experimental solutions with different concentrations of 0.002 and 0.005 mol/L. Note that all operations related to highly corrosive and toxic reagents should be carried out in a fume hood and the operators must be protected by wearing protective equipment during the whole experimental process.

The experiments were performed using Tuttle-type cold-seal pressure vessels with a 27 mm outer diameter, a 6 mm inner diameter, and a 250 mm length, which is suitable for high temperature–pressure experiments up to 950 °C and 500 MPa at the hydrothermal laboratory of the Guangzhou Institute of Geochemistry, China [25–29]. The pressure was transmitted by the deionized water and monitored with a high-precision high-pressure gauge ($\pm$5 MPa). The temperature was controlled by the heating furnace and measured with a high-accuracy electronic temperature controller ($\pm$5 °C) using a NiCr-Ni (K-type) thermocouple. A constant-temperature drying oven ($\pm$1 °C, DGG-9070B, Jiangdong, China) was used to process the experimental products.

The analysis equipment used in this study included a field-emission scanning electron microscope (SEM) equipped with an energy-dispersive spectrometer (EDS), a high-resolution confocal Raman spectrometer, and a micro-area X-ray Diffraction (µ-XRD). The field-emission scanning electron microscope (SEM) (SU8010, HITACHI, Tokyo, Japan) and an EDAX Apollo x-SDD energy dispersive spectrometer (EDS) (Core Lab, Tulsa, OK, USA) were used for morphological and composition analysis of the crystals with a working voltage of 15 kV and a magnification of 600–80,000 at the State Key Laboratory of Organic Geochemistry of the Guangzhou Institute of Geochemistry, China [26]. The high-resolution confocal Raman spectrometer (alpha 300R, WITec Instruments Corp, Ulm, Germany) was equipped with three lasers (488, 532, and 633 nm), three gratings (300, 600, and 1800 grooves/mm), and four Zeiss objectives (5×, 20×, 50×, and 100×) and was used for the qualitative analysis of the crystals with a laser power of 10 mW, an integration time of 6 s, and a laser wavelength of 532 nm at the hydrothermal laboratory of Guangzhou Institute of Geochemistry, China [30]. A Dmax RAPID V micro-area X-ray Diffraction (µ-XRD) (Rigaku, Tokyo, Japan) with a working voltage of 40 kV, working current of 30 mA, exposure time of 100 s, and collimator of 0.1 mm was used for the structure analysis of the crystals at the CAS Key Laboratory of Mineralogy and Metallogeny of the Guangzhou Institute of Geochemistry, China.

2.2. Experimental Process

Firstly, gold capsules with a diameter of 5 mm and a length of 20–30 mm were prepared by acid boiling, quenching, and cleaning with deionized water and ethanol and was used as the sample reactant container. Then, the container was filled with the initial experimental solutions accounting for 40–60% of the volume and sealed at both ends with a tungsten

inert gas welding system (PUK U3, Germany). Next, the sample reactant container was placed into the Tuttle-type cold-seal pressure vessels and followed by a nickel filler rod to prevent the sample reactant container from bobbing due to heating. After the experiments were finished, the vessels were quickly quenched in an ice–water mixture to drop the temperature to below 100 °C in several seconds. Finally, the sample reactant container was taken out from the cold-seal pressure vessels and then unfolded, cleaned repeatedly with deionized water and alcohol, and dried for analysis. Note that before and after all experiments, the capsule was checked for leaks by weighing and heating.

3. Results and Discussion

K_2OsCl_6 can remain stable at room temperature and ambient pressure but gradually hydrolyzes and eventually forms a precipitate at high temperature and high pressure [31]. The cumulative hydrolysis reaction and formation of OsO_2 crystal can be expressed as:

$$K_2OsCl_6(aq) + 2H_2O \rightarrow OsO_2(s) + 4HCl(aq) + 2\,KCl(aq) \tag{1}$$

The above reaction can occur rapidly and precipitate within a few hours, producing OsO_2 crystals, hydrochloric acid, and chloride ions to create an acidic and chlorine-bearing environment [27]. All experiments were performed at a pressure of 100 MPa to avoid the effect of pressure on the OsO_2 crystals. The experimental products were identified as OsO_2 precipitates by the EDS (Figure 1) and the Raman spectrum (Figure 2). Moreover, the XRD spectra also showed that the crystals at 150 and 550 °C, 24 h, and 100 MPa using the 0.005 mol/L initial solution were OsO_2, indicating that the experimental products from 150 to 550 °C were OsO_2 crystals (Figure 3). All the identifications indicated that the experimental products were OsO_2 crystals. The morphology of the OsO_2 precipitates was analyzed with the SEM, which clearly shows that the OsO_2 crystals were in the form of nanospheres or irregular nanoparticles with a diameter of 40–500 nm at different magnifications (Figures 4 and 5). All experimental conditions and the results of OsO_2 crystals are shown in Table 1.
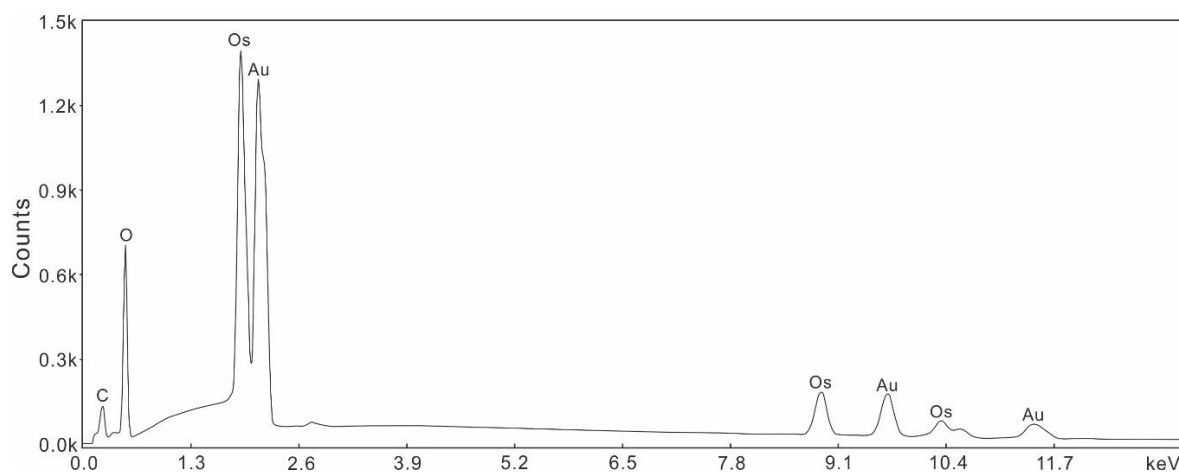

Figure 1. Representative EDS analysis of OsO_2 adhered to the inner surface of the gold capsule. Note that Au is derived from the gold capsule.
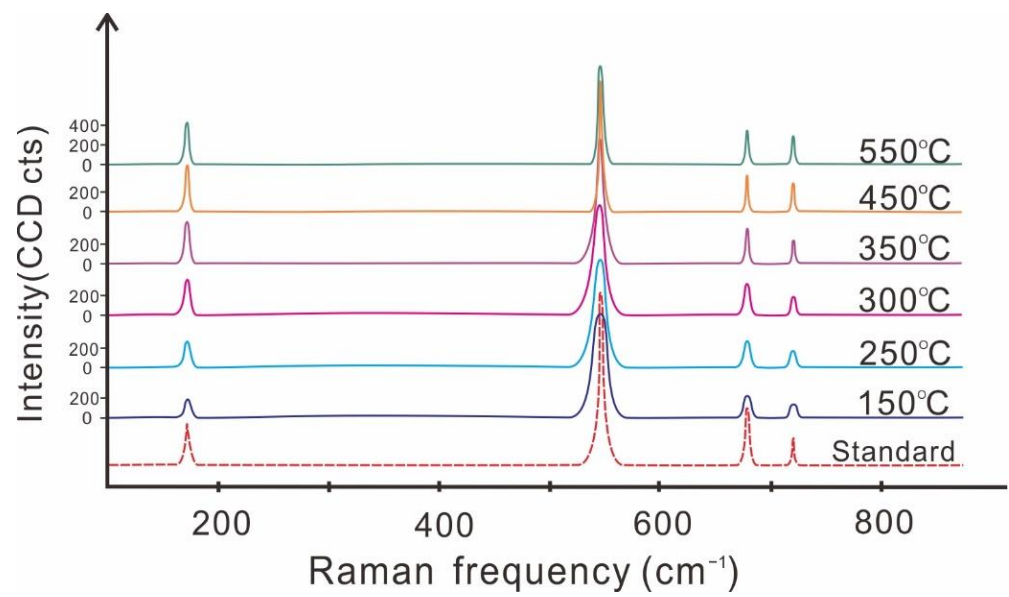
Figure 2. Raman spectra of OsO_2 in the present study and typical OsO_2 crystals. The standard Raman spectrum of OsO_2 is derived from Yen, et al. [32].
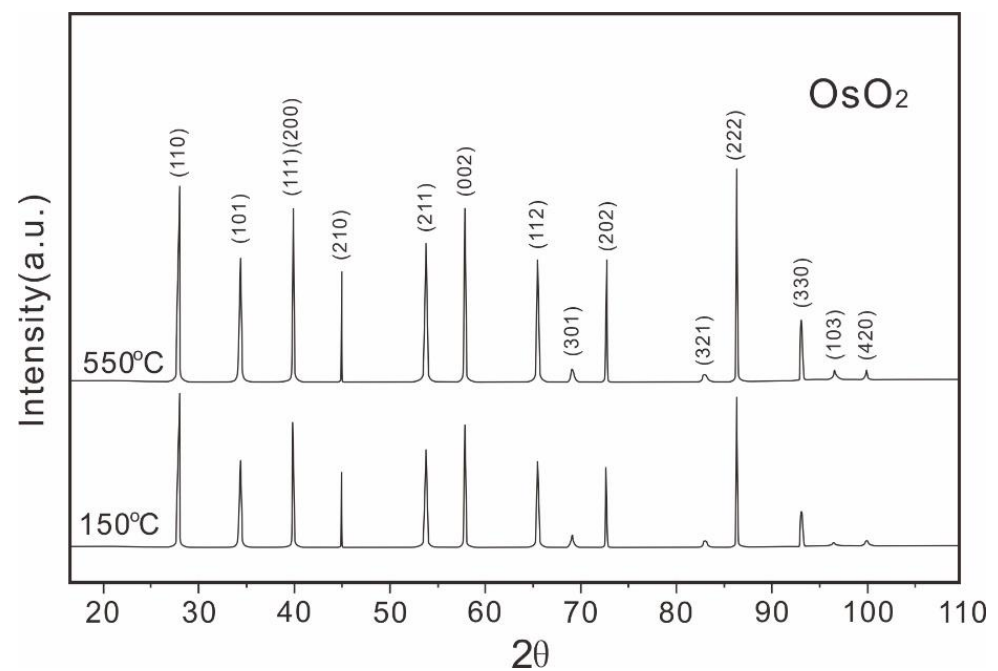

Figure 3. Representative XRD analysis of the OsO_2 crystals at 150 and 550 °C, 24 h, and 100 MPa using 0.005 mol/L initial solutions.
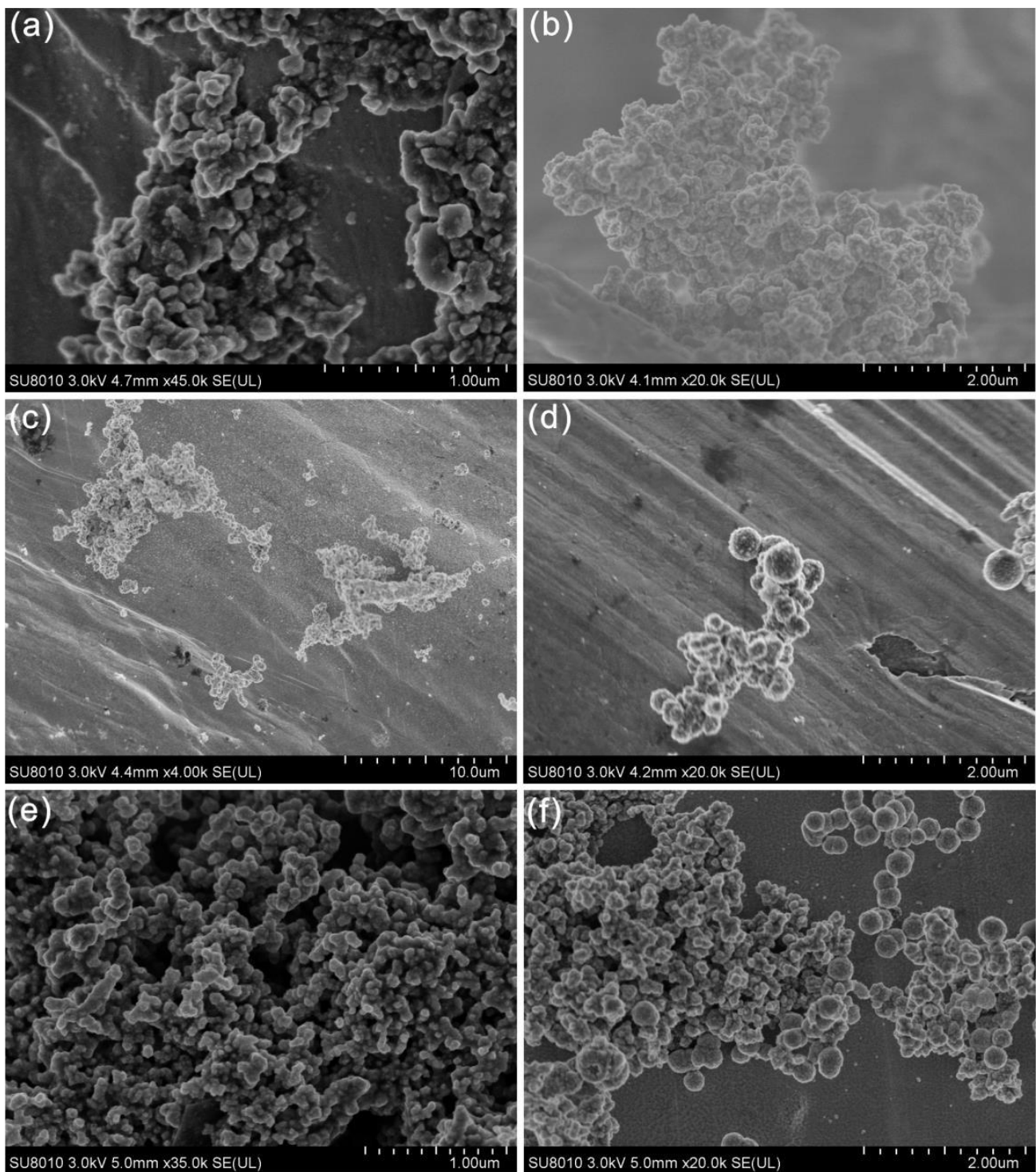
Figure 4. Representative SEM micrographs of OsO_2 nanospheres using 0.002 mol/L initial solution for: (**a**) No. 1 at 300 °C, 100 MPa, and 5 h; (**b**) No. 2 at 300 °C, 100 MPa, and 12 h; (**c**) No. 3 at 300 °C, 100 MPa, and 24 h; (**d**) No. 4 at 300 °C, 100 MPa, and 36 h; (**e**) No. 5 at 250 °C, 100 MPa, and 24 h; and (**f**) No. 6 at 450 °C, 100 MPa, and 24 h.
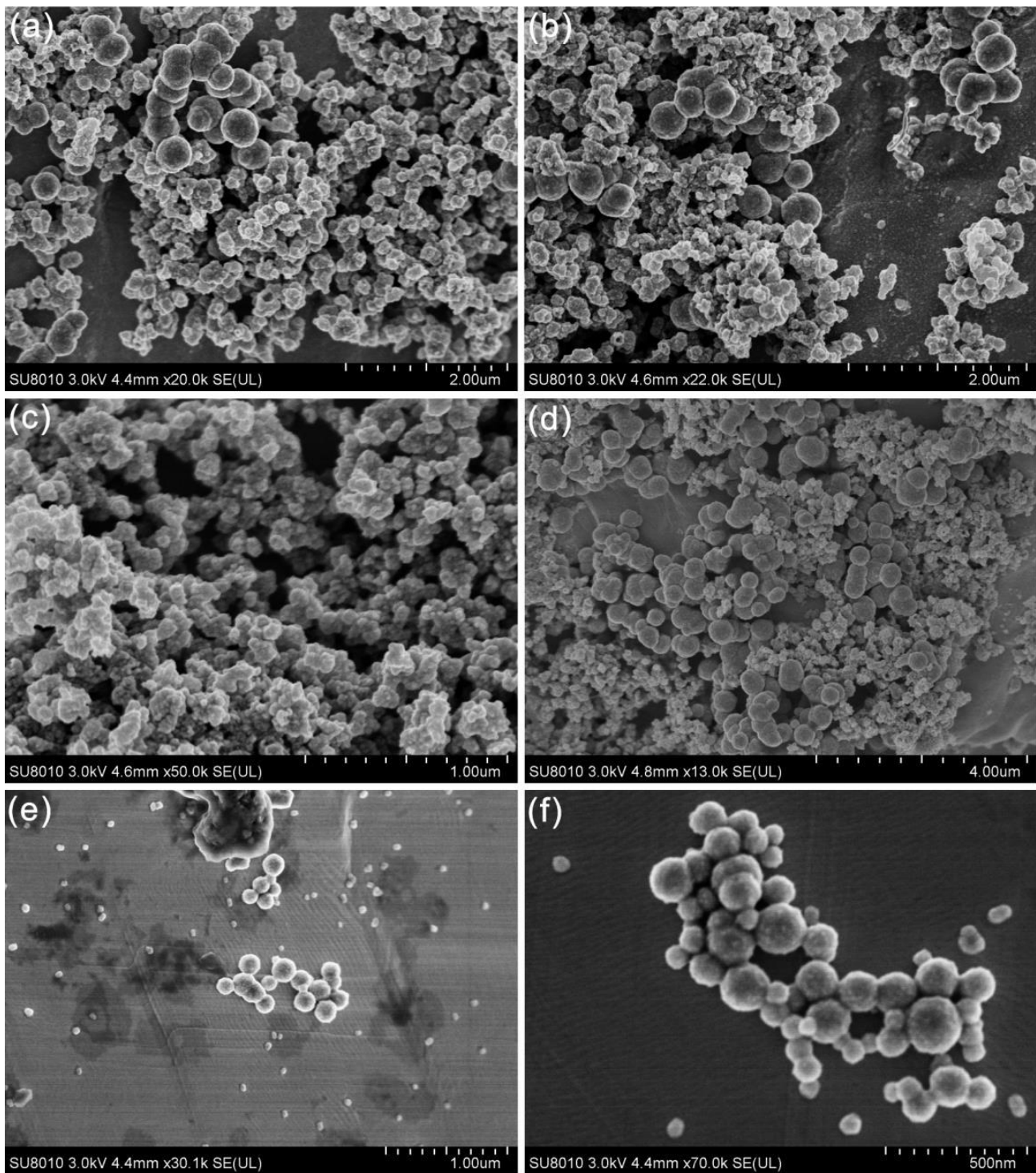
Figure 5. Representative SEM micrographs of OsO_2 nanospheres using 0.005 mol/L initial solution for: (**a**) No. 7 at 150 °C, 100 MPa, and 24 h; (**b**) No. 8 at 250 °C, 100 MPa, and 24 h; (**c**) No. 9 at 350 °C, 100 MPa, and 24 h; (**d**) No. 10 at 450 °C, 100 MPa, and 24 h; and (**e**,**f**) No. 11 at 550 °C, 100 MPa, and 24 h.

Table 1. Preparation of the OsO_2 nanospheres under various conditions.

No.	Initial K_2OsCl_6 Concentration (mol/L)	Temperature (°C)	Pressure (MPa)	Time (h)	Diameter (nm)
1	0.002	300	100	5	40–150
2	0.002	300	100	12	100–280
3	0.002	300	100	24	100–380
4	0.002	300	100	36	150–450
5	0.002	250	100	24	50–150
6	0.002	450	100	24	100–400
7	0.005	150	100	24	50–400
8	0.005	250	100	24	100–400
9	0.005	350	100	24	50–200
10	0.005	450	100	24	100–500
11	0.005	550	100	24	50–300

3.1. Time Effect on the OsO_2 Crystals

Time series experiments showed that the hydrolysis time provides direct constraints on the crystal structure and size of OsO_2 precipitates. As shown in Figure 4a–d, at 300 °C, 100 MPa, and 0.002 mol/L initial solution, the OsO_2 crystals were in the form of irregular nanoparticles and grew from the diameter of 40–150 nm to the diameter of 100–280 nm when the time was increased from 5 to 12 h. When the time was increased from 12 to 24 h, the OsO_2 crystals grew from irregular nanoparticles with a diameter of 100–280 nm to nanosphere crystals with 100–380 nm in size. As time was elevated from 24 to 36 h, the OsO_2 crystals increased in size from 100–380 nm to 150–450 nm, presenting as nanosphere OsO_2 crystals. These data indicated that the OsO_2 crystals can grow from irregular nuclei to nanospheres with time. The OsO_2 crystals tended to be complete nanosphere crystals after 24 h, as the hydrolysis reaction can reach equilibrium within 24 h, according to previous studies [25,27]. Hence, all following experiments were performed for 24 h to ensure the integrity of the OsO_2 nanosphere crystals.

Given that the size of the OsO_2 crystals could be increased with time at similar conditions of 300 °C, 100 MPa, and 0.002 mol/L initial solution concentration, the growth rate of the OsO_2 crystals could be estimated by counting the sizes of OsO_2 crystals at various timepoints, as shown in Figure 6. The results showed that the growth rate of OsO_2 crystals reached 18.6 nm/h before 12 h, dropped to 8.3 nm/h from 12–24 h, and was only 5.8 nm/h after 24 h, which can be mainly attributed to the hydrolysis rate of K_2OsCl_6. The hydrolysis rate of K_2OsCl_6 reaches a maximum value within 12 h because of the promotion of a high initial K_2OsCl_6 concentration for reaction (1), resulting in the rapid growth of OsO_2 crystals within the first 12 h. Then, the hydrolysis rate decreases after 12 h due to the decreasing initial Os concentration and the elevated concentrations of HCl and KCl in the aqueous solution, which reduces the reaction (1) rate and causes a decrease in the growth rate of OsO_2 crystals after 12 h. Finally, after the hydrolysis reaction reaches an equilibrium, the Os concentration in the aqueous solution remains stable, meaning that there exists a dynamic equilibrium between the Os concentration in the aqueous solution and the precipitated OsO_2, which further reduces the growth rate of OsO_2 crystals [29,33,34]. Accordingly, the morphology results at various timepoints suggested that the OsO_2 crystals gradually precipitated from the solution and clumped together to form irregular crystals before the equilibrium of the experimental reaction due to the sudden precipitation of a large amount of OsO_2 products in a short period. However, when the hydrolysis reaction reached equilibrium, OsO_2 was in the form of a complete nanosphere crystal and grew slowly in size with increasing time.
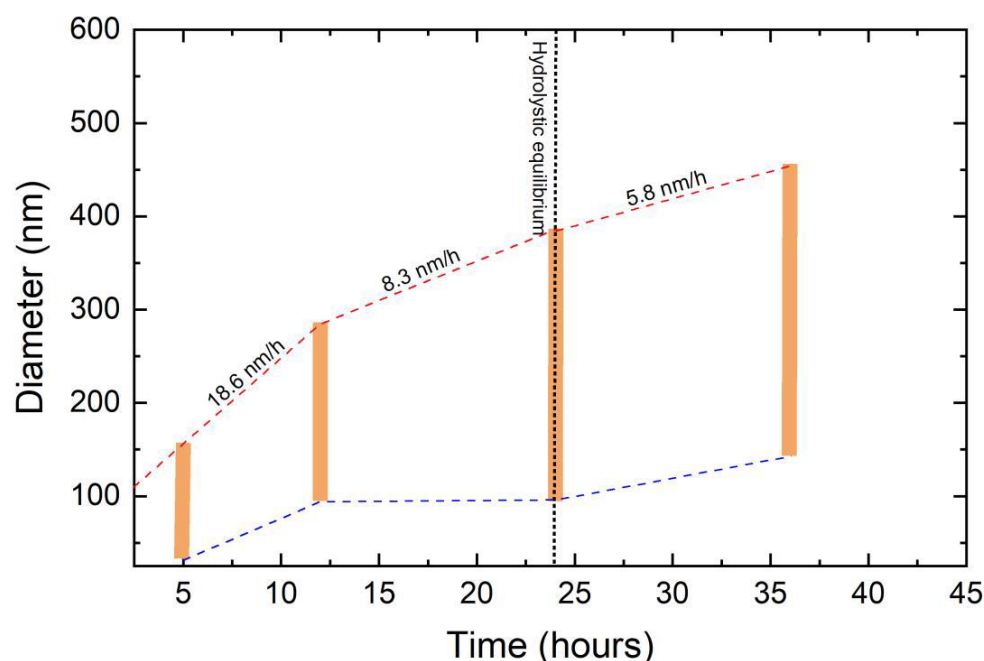
Figure 6. Grain size diagram of OsO$_2$ nanospheres from various timepoints synthesized at 300 °C and 100 MPa using 0.002 mol/L initial solution.

3.2. Temperature Dependence on the OsO$_2$ Crystals

The experimental temperature significantly affects the growth and morphology of OsO$_2$ crystals, based on the morphology results from SEM. As expounded by previous studies, the temperature can affect the degree of the hydrolysis reaction and thus restrict the morphology of hydrolysis products [26,35,36]. In this study, the temperature presented an obvious restriction on the morphology of OsO$_2$. The OsO$_2$ grew from 50–150 nm to 100–380 nm to 100–400 nm and was more uniform with temperature increasing from 250 °C to 300 °C to 450 °C at low initial concentrations solution of 0.002 mol/L and 100 MPa (Figure 4c,e–f). As shown in Figure 5, at the high initial concentration of 0.005 mol/L initial solution, 100 MPa, and 24 h, the OsO$_2$ was in either the form of small nanospheres or irregular nanospheres with a diameter of 50–400 nm at 150 °C (Figure 5a) and a diameter of 100–400 nm at 250 °C (Figure 5b). OsO$_2$ presented as 50–200 nm nanosphere crystals at 350 °C (Figure 5c) but became more uniform and complete nanospheres with sizes of 100–500 nm at 450 °C (Figure 5d) and 50–300 nm at 550 °C (Figure 5e,f). As the result of the morphology of the OsO$_2$ crystals at varying temperatures, the crystal structure of OsO$_2$ became more uniform and complete when the temperature increased from 150 to 550 °C.

Building upon the statistics for the size of the OsO$_2$ nanosphere crystals at different temperatures, the size of OsO$_2$ crystals as a whole showed a gradual increase from 160–185 to 215–240 nm when temperatures were elevated from 150 to 550 °C, indicating that elevated temperature has a positive effect on the size of the OsO$_2$ crystals (Figure 7). The results show that the OsO$_2$ crystals gradually increased in size from 160–185 to 185–210, 215–240, and 215–240 nm when temperatures were elevated from 150 to 250, 450, and 550 °C, respectively. This shows that temperature has a promoting effect on the growth of the OsO$_2$ crystals. However, the OsO$_2$ crystals at 350 °C had a more uniform size but smaller diameter than that of other temperatures, for which a possible slight oscillation of the experimental process and the difference in the statistical region may be responsible. Hence, the effect of temperature on the morphology of OsO$_2$ nanosphere crystals can be explained by the hydrolysis process of K$_2$OsCl$_6$. Elevated temperature can promote reaction (1) and increase the reaction rate of ions and molecules, further resulting in a large amount of OsO$_2$ being precipitated from the solution and the growth of OsO$_2$ crystals in size [37].
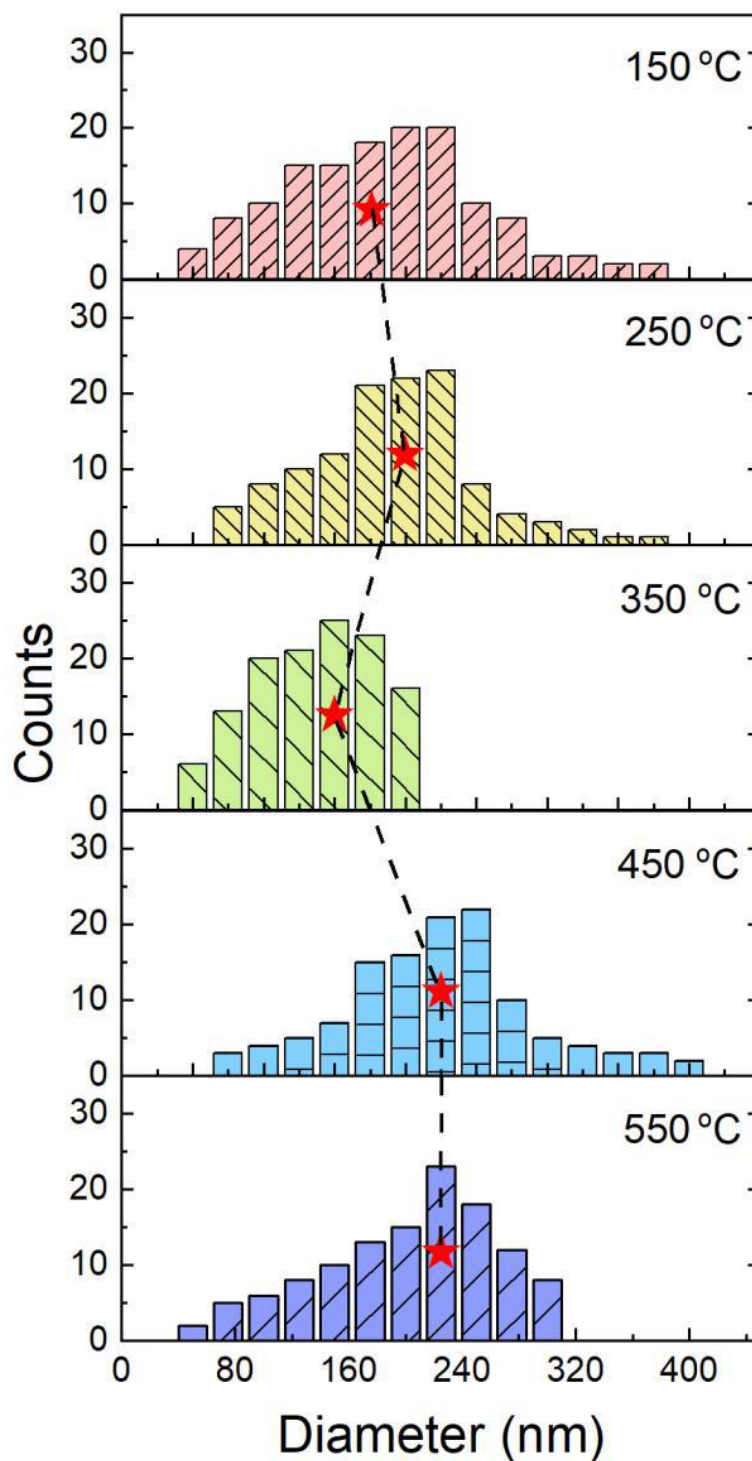
Figure 7. Statistical histograms of diameter sizes for OsO$_2$ nanospheres at 150–550 °C, 100 MPa, and 24 h in the 0.005 mol/L initial solution. Note that the asterisk represents the median of counts of different temperatures.

3.3. The Influence of Initial Solution Concentration on the OsO$_2$ Crystals

Besides time and temperature, the initial solution concentration also has an essential influence on the morphology of OsO$_2$ crystals. As shown in Figures 4e and 5b, at the same experimental conditions of 250 °C, 24 h, and 100 MPa, the OsO$_2$ crystals grew from 50–150 nm irregular nanospheres at 0.002 mol/L initial solution to a 100–400 nm nanospheres or irregular nanospheres at 0.005 mol/L initial solution. At the higher temper-

ature of 450 °C, the OsO_2 nanosphere crystals were also larger when using the 0.005 mol/L initial solution (a diameter of 100–500 nm) than those of the lower initial concentration solution of 0.002 mol/L (a diameter of 100–400 nm) (Figures 4f and 5d). These results suggest that the initial solution concentration has a positive effect on the growth of the OsO_2 crystals in size, which could be attributed to the promotion of high initial K_2OsCl_6 concentrations for the occurrence of reaction (1) and the formation of a large amount of OsO_2 precipitates during the process of hydrolysis.

3.4. The Growth Mechanism of the OsO_2 Nanosphere Crystals

Crystal nucleation and aggregate growth are usually complex processes involving the combination of atoms, particle aggregation, nucleation, and ordered combination of crystal nuclei [38,39]. In this study, with the experimental time increasing from 5 to 24 h before equilibrium, reaction (1) occurs and produces a large amount of OsO_2 precipitates. Then, the OsO_2 precipitates quickly aggregate and nucleate to form irregular nanoparticles and gradually grow, displaying a series of idiomorphic and other-shaped OsO_2 nanoparticles in the chlorine-bearing fluids (Figure 4a–c). This suggests that the growth of OsO_2 is similar to the formation mechanism of early pyrite and rutile crystals and follows the nucleation and aggregate growth pattern before the equilibrium of the hydrolysis reaction [33,40,41]. Therefore, the nucleation and aggregate growth pattern could mainly control the formation and growth of the OsO_2 crystals.

When reaction (1) is close to or reaches the equilibrium, the OsO_2 precipitates are in a dynamic equilibrium of dissolution and precipitation. The OsO_2 exist as irregular nanoparticles and nanospheres with a wide diameter of 100–450 nm and grow gradually with time (Figure 4c–f). The process can mainly be explained by Ostwald ripening, rather than the nucleation and aggregate growth of crystals [33,42–45]. Under the dynamic equilibrium of OsO_2 precipitates and the dissolution of chlorine in the hydrothermal fluids, the OsO_2 precipitates from the reactive fluids were significantly reduced. At this time, the nucleation and aggregate growth pattern had a weak effect on the growth of the OsO_2 crystals. Being in the dynamic equilibrium, the small OsO_2 nanoparticles synthesized early gradually dissolved and decreased, while the large OsO_2 nanospheres gradually increased and grew in this study (Figures 4 and 5). Furthermore, as shown in Figure 8, at 300 °C, 100 MPa, and 0.002 mol/L initial solution, the maximum diameter of OsO_2 crystals increased with time and is entirely consistent with the growth curve of Ostwald ripening. These conclusions provide direct evidence that the Ostwald ripening dominates the formation and growth of the OsO_2 nanospheres with time. They also showed that the OsO_2 crystals' growth is controlled by the diffusion of Os ions along the fluid–nanoparticle boundary, according to the fitting equation in Figure 8 [42]. The result from Figure 8 shows that the Ostwald ripening not only controls the growth of OsO_2 crystals on a long time scale but could also play a role in the growth of OsO_2 crystals before the hydrolysis reaction reaches equilibrium. Thus, Ostwald ripening dominates the growth of OsO_2 crystals when the hydrolysis reaction reaches equilibrium, but imparts a limited effect on the occurrence of the OsO_2 crystals on a short time scale. Certainly, high temperature and initial concentration push the reaction (1) to the right, form a large amount of OsO_2 precipitates, and produce a large amount of chlorine in the hydrothermal fluids, further promoting the Ostwald ripening of the OsO_2 crystals and the occurrence of OsO_2 nanosphere crystals (Figures 4e,f and 5). Moreover, OsO_2 nanosphere crystals are obtained for the first time and likely have great application potential as microbial reagents, catalysts, gas fixing agents, and electrode conductivity materials because of their high surface area and good electrode conductivity [19–22].
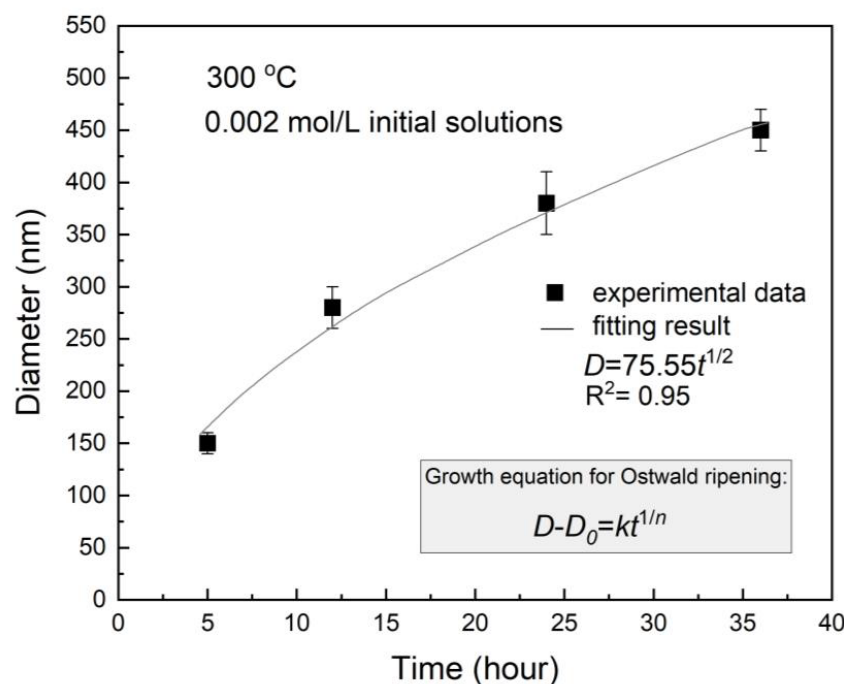
Figure 8. Experimental data and fitting results showing maximum diameter sizes of OsO_2 crystals vs. time at 300 °C and 100 MPa in 0.002 mol/L initial solutions.

3.5. Geological Implication

The crystal morphology of minerals is related to their growth process and environments and thus can be used as a tracer to indicate their growth environments, just as with hydrothermal pyrite, whose morphology is related to the hydrothermal temperature and properties [46,47]. Given that Os is usually stable and transported as a high coordination chloride complex, such as $OsCl_6^{2-}$, in the deep sea—though these complexes could hydrolyze and precipitate to form crystals—the morphology of OsO_2 crystals could shed light on the unique environment for the growth of OsO_2 crystals [48,49]. As mentioned in previous studies, only the rutile-type OsO_2 crystal has been synthesized by the chemical-vapor-transport (CVT) method and is related to the high synthesis temperature (800–940 °C) and oxygen-rich environment [18,24]. Different from the synthesis method of rutile-type OsO_2 crystals in the gaseous phase, the OsO_2 nanosphere crystals were synthesized by the hydrolysis of the Os–chloride complex for the first time in this study and could be related to the oxidized hydrothermal fluids in terms of the existence of high-valence Os. Moreover, the homogeneity of the OsO_2 nanosphere crystals in this study shows a stable hydrothermal fluid environment [50]. The OsO_2 crystals in the form of nanospheres instead of a rutile-type form in this study may be due to the dissolution of chlorine, low temperature, high pressure, and low Os saturation in hydrothermal fluids [18,48,51]. The lower temperature and higher pressure may not allow the OsO_2 crystal to completely grow according to a lattice structure [51]. The dissolution of chlorine and the low Os saturation also prevented the OsO_2 crystals from growing a rutile-type structure. In this case, the OsO_2 nanosphere crystals could occur in this study. Furthermore, the growth process of OsO_2 crystals in this study is closely related to the stability and hydrolysis of the Os–chloride complex in hydrothermal fluids and could indirectly trace the transport and cycle of Os as the Os–chloride complex from the magmatic process to the hydrothermal system [14]. Based on the growth mechanism of the OsO_2 crystals and the hydrolysis behavior of K_2OsCl_6, OsO_2 nanospheres could occur in relatively acidic chlorine-rich oxidized hydrothermal environments [27]. For example, they could occur in the ocean-floor sediments and muds near hydrothermal vents due to the favorable growth conditions for OsO_2 nanosphere crystals [7,52,53]. Accordingly, the growth of OsO_2 nanosphere crystals may be used as the typomorphic mineral to trace the hydrothermal conditions and fluid properties.

4. Conclusions

According to the hydrolysis experiments of K_2OsCl_6 with temperatures from 150 to 550 °C, times from 5 to 36 h, initial solution concentrations from 0.002 to 0.005 mol/L, and 100 MPa water pressure, this study obtained OsO_2 nanosphere crystals with a diameter of 40–500 nm. With time increasing from 5 to 36 h at 300 °C, 100 MPa, and 0.002 mol/L initial solution, the OsO_2 crystals varied from irregular nanoparticles to nanospheres and grew from 40–150 nm to 150–450 nm in size. As the temperature increases, the OsO_2 nanosphere crystals became more uniform and larger due to the promotion of the hydrolysis of the Os–chloride complex, attributed to high temperature. High initial solution concentrations precipitate more OsO_2 precipitates and promote the growth of the OsO_2 crystals. These conclusions suggest that the growth of the OsO_2 nanosphere crystals in the aqueous solution is complex and is mainly controlled by the nucleation and aggregate growth pattern before the hydrolysis reaction reaches the equilibrium but is dominated by the Ostwald ripening during the whole process of growth, especially after the equilibrium. According to the high surface area and good electrode conductivity, The OsO_2 nanosphere crystals may have great application potential as microbial reagents, catalysts, electrode conductivity materials, and in other fields. Based on the relationship between the morphology and size of OsO_2 crystals and the experimental conditions, this study considered that the OsO_2 nanosphere crystals could be a typomorphic mineral for hydrothermal vent systems and provide an indirect understanding of the transport and enrichment of Os in the form of Os–chloride complexes in seafloor hydrothermal systems.

References

1. Brantley, S.L.; Kubicki, J.D.; White, A.F. *Kinetics of Water-Rock Interaction*; Springer Science+Business: New York, NY, USA, 2008; pp. 1–825.
2. Hyndman, R.D.; Peacock, S.M. Serpentinization of the forearc mantle. *Earth Planet. Sci. Lett.* **2003**, *212*, 417–432. [CrossRef]
3. Mével, C. Serpentinization of abyssal peridotites at mid-ocean ridges. *C. R. Geosci.* **2003**, *335*, 825–852. [CrossRef]
4. Charlou, J.L.; Fouquet, Y.; Bougault, H.; Donval, J.P.; Rona, P.A. Intense ch4 plumes generated by serpentinization of ultramafic rocks at the intersection of the 15°20′ N fracture zone and the mid-atlantic ridge. *Geochim. Cosmochim. Acta* **1998**, *62*, 2323–2333. [CrossRef]
5. Lowell, R.P.; Rona, P.A.; von Herzen, R.P. Seafloor hydrothermal systems. *J. Geophys. Res. Solid Earth* **1995**, *100*, 327–352. [CrossRef]
6. Kurian, P.J.; Rajan, S.; Agarwal, D.K.; Linsy, P. Indian Ocean Ridge System and Seafloor Hydrothermal Activity. *J. Geol. Soc. India* **2022**, *98*, 155–164. [CrossRef]
7. Huang, W.; Li, J.; Tao, C.H.; Sun, Z.L.; He, Y.J.; Cui, N.Y. PGE characteristics of sulfide chimney bodies in hydrothermal regions, Southwest Indian ridge 49°39′ E. *Acta Miner. Sin.* **2011**, *31* (Suppl. 1), 691. (In Chinese)
8. Sun, Z.; Zhou, H.; Glasby, G.P.; Sun, Z.; Yang, Q.; Yin, X.; Li, J. Mineralogical characterization and formation of Fe-Si oxyhydroxide deposits from modern seafloor hydrothermal vents: American Mineralogist. *Acta Physiol. Pol.* **2013**, *32*, 407–417. [CrossRef]
9. Sun, K.C.; Sang, J.P.; Kim, J.; Park, J.W.; Son, S.K. Gold and tin mineralisation in the ultramafic-hosted Cheoeum vent field, Central Indian Ridge. *Miner. Depos.* **2021**, *56*, 885–906.
10. Ren, J.B.; He, G.W.; Yao, H.Q.; Zhang, H.D.; Yang, S.X.; Deng, X.G.; Zhu, K.C. Geochemistry and Significance of REE and PGE of the Cobalt-Rich Crusts from West Pacific Ocean Seamounts. *Earth Sci.* **2016**, *41*, 1745–1757. (In Chinese with English abstract) [CrossRef]

11. Liu, Y.J.; Cao, L.M.; Li, Z.L.; Wang, H.N.; Chu, T.Q.; Zhang, J.R. *Elemental Geochemistry*; Science Press: Beijing, China, 1984; pp. 1–548. (In Chinese)

12. Guan, Y.; Jiang, X.D.; Zhou, L.; Sun, X.M. Geochemical characteristics of polymetallic crusting (nuclear) platinum group element (PGE) in the South China Sea. *Miner. Depos.* **2014**, *33*, 625–626. [CrossRef]

13. Gao, J.J.; Liu, J.H.; Zhang, H.; Yan, S.J.; He, L.H.; Wang, X.J.; Wang, H.M. Occurrence phase and enrichment mechanism of platinum group elements in the Pacific cobalt-rich crusts. *Haiyang Xuebao* **2019**, *41*, 115–124. (In Chinese with English abstract) [CrossRef]

14. Sun, X.M.; Xue, T.; He, G.W.; Zhang, M.; Shi, G.Y.; Wang, S.W.; Lu, H.F. Platinum group elements (PGE) and Os isotopic geochemistry of ferromanganese crust from Pacific Ocean seamounts and their constrains on genesis. *Acta Petrol. Sin.* **2006**, *22*, 3014–3026. (In Chinese with English abstract)

15. Wang, C.Y.; Zhou, M.F.; Qi, L. Origin of extremely PGE-rich mafic magma system: An example from the Jinbaoshan ultramafic sill, Emeishan large igneous province, SW China. *Lithos* **2010**, *119*, 147–161. [CrossRef]

16. Wang, C.Y.; Prichard, H.M.; Zhou, M.F.; Fisher, P.C. Platinum-group minerals from the Jinbaoshan Pd–Pt deposit, SW China: Evidence for magmatic origin and hydrothermal alteration. *Miner. Depos.* **2008**, *43*, 791. [CrossRef]

17. Pašava, J.; Vymazalová, A.; Petersen, S.; Herzig, P. PGE distribution in massive sulfides from the P ACMANUS hydrothermal field, eastern Manus basin, Papua New Guinea: Implications for PGE enrichment in some ancient volcanogenic massive sulfide deposits. *Miner. Depos.* **2004**, *39*, 784–792. [CrossRef]

18. Yen, P.C.; Chen, R.S.; Chen, C.C.; Huang, Y.S.; Tiong, K.K. Growth and characterization of OsO_2 single crystals. *J. Cryst. Growth* **2004**, *262*, 271–276. [CrossRef]

19. Graebner, J.E.; Greiner, E.S.; Ryden, W.D. Magnetothermal oscillations in RuO_2, OsO_2, and IrO_2. *Phys. Rev. B* **1976**, *13*, 2426–2432. [CrossRef]

20. Mattheiss, L.F. Electronic structure of RuO_2, OsO_2, and IrO_2. *Phys. Rev. B* **1976**, *13*, 2433–2450. [CrossRef]

21. Hayakawa, Y.; Kohiki, S.; Arai, M.; Yoshikawa, H.; Fukushima, S.; Wagatsuma, K.; Oku, M.; Shoji, F. Electronic structure and electrical properties of amorphous OsO_2. *Phys. Rev. B* **1999**, *59*, 11125. [CrossRef]

22. Heidari, A.; Hotz, M.; MacDonald, N.; Peterson, V.; Caissutti, A.; Besana, E.; Esposito, J.; Schmitt, K.; Chan, L.-Y.; Sherwood, F.; et al. Osmium Dioxide (OsO_2) and Osmium Tetroxide (OsO_4) Smart Nano Particles, Nano Capsules and Nanoclusters Influence, Impression and Efficacy in Cancer Prevention, Prognosis, Diagnosis, Imaging, Screening, Treatment and Management under Synchrotron and Synchrocyclotron Radiations. *Int. J. Phys.* **2022**, *10*, 1–22.

23. Horkans, J.; Shafer, M.W. An Investigation of the Electrochemistry of a Series of Metal Dioxides with Rutile-Type Structure: MoO_2, WO_2, ReO_2, RuO_2, OsO_2, and IrO_2. *J. Electrochem. Soc.* **1977**, *124*, 1202–1207. [CrossRef]

24. Yen, P.C.; Chen, R.S.; Chen, C.C.; Huang, Y.S.; Tiong, K.K.; Liao, P.C. Preparation and Characterization of OsO_2. *J. Alloys Compd.* **2004**, *383*, 277–280. [CrossRef]

25. Yan, H.B.; He, J.J.; Liu, X.W.; Wang, H.B.; Liu, J.F.; Ding, X. Thermodynamic Investigation of the Hydrolysis Behavior of Fluorozirconate Complexes at 423.15–773.15 K and 100 MPa. *J. Solut. Chem.* **2020**, *49*, 836–848. [CrossRef]

26. Yan, H.B.; Di, J.; Li, J.; Liu, Z.; Liu, J.; Ding, X. Synthesis of Zirconia Micro-Nanoflakes with Highly Exposed (001) Facets and Their Crystal Growth. *Crystals* **2021**, *11*, 871. [CrossRef]

27. Yan, H.B.; Sun, W.D.; Liu, J.F.; Tu, X.L.; Ding, X. Thermodynamic properties of ruthenium (IV) chloride complex and the transport of ruthenium in magmatic-hydrothermal fluids. *Ore Geol. Rev.* **2021**, *131*, 104043. [CrossRef]

28. He, J.J.; Ding, X.; Wang, Y.R.; Sun, W.D. The effect of temperature and concentration on hydrolysis of fluorine-rich titanium complexes in hydrothermal fluids: Constraints on titanium mobility in deep geological processes. *Acta Petrol. Sin.* **2015**, *31*, 802–810. (In Chinese with English abstract)

29. He, J.J.; Ding, X.; Wang, Y.R.; Sun, W.D. The effects of precipitation-aging-re-dissolution and pressure on hydrolysis of fluorine-rich titanium complexes in hydrothermal fluids and its geological implications. *Acta Petrol. Sin.* **2015**, *31*, 1870–1878. (In Chinese with English abstract)

30. Zhang, L.; Wang, Q.; Ding, X.; Li, W.C. Diverse serpentinization and associated abiotic methanogenesis within multiple types of olivine-hosted fluid inclusions in orogenic peridotite from northern Tibet. *Geochim. Cosmochim. Acta* **2021**, *296*, 1–17. [CrossRef]

31. Ding, X.; Harlov, D.E.; Chen, B.; Sun, W.D. Fluids, Metals, and Mineral/Ore Deposits. *Geofluids* **2018**, *2018*, 1452409. [CrossRef]

32. Yen, P.C.; Chen, R.S.; Huang, Y.S.; Chia, C.T.; Chen, R.H.; Tiong, K.K. The first-order Raman spectra of OsO_2. *J. Phys. Condens. Matter* **2003**, *15*, 1487–1494. [CrossRef]

33. Ding, X.; He, J.J.; Liu, Z.Y. Experimental Studies on Crystal Growth of Anatase under Hydrothermal Conditions. *Earth Sci.* **2018**, *43*, 1763–1772.

34. Grzybkowski, W. Nature and properties of metal cations in aqueous solutions. *Pol. J. Environ. Stud.* **2006**, *15*, 655–663.

35. Di, J.; Yan, H.B.; Liu, Z.Y.; Ding, X. Synthesis and Characterization of Anatase TiO_2 Microspheres Self-Assembled by Ultrathin Nanosheets. *Materials* **2021**, *14*, 2870. [CrossRef] [PubMed]

36. Wang, Y.R.; Chou, I.M. Characteristics of hydrolysis of the complex Na2SnF6 in hydrothermal solutions—An experimental study. *Chin. J. Geochem.* **1987**, *6*, 372–382. [CrossRef]

37. Mo, J.X. Impact on Chemistry Reaction Speed, Balance and Conversion Ratio of Temperature. *High. Educ. Forum* **2004**, *5*, 161–164. (In Chinese with English abstract)

38. Lee, G.S.; Lee, Y.J.; Yoon, K.B. Layer-by-Layer Assembly of Zeolite Crystals on Glass with Polyelectrolytes as Ionic Linkers. *J. Am. Chem. Soc.* **2001**, *123*, 9769–9779. [CrossRef]

39. Yoreo, J.J.D.; Gilbert, P.U.P.A.; Sommerdijk, N.A.J.M.; Penn, R.L.; Whitelam, S.; Joester, D.; Zhang, H.; Rimer, J.D.; Navrotsky, A.; Banfield, J.F.; et al. Crystallization by particle attachment in synthetic, biogenic, and geologic environments. *Science* **2015**, *349*, aaa6760. [CrossRef] [PubMed]

40. Wang, F.D.; Richards, V.N.; Shields, S. Kinetics and Mechanisms of Aggregative Nanocrystal Growth. *Chem. Mater.* **2014**, *26*, 5–21. [CrossRef]

41. Xian, H.Y.; Zhu, J.X.; Tang, H.M. Aggregative Growth of Quasi-Octahedral Iron Pyrite Mesocrystals in Polyol Solution through Oriented Attachment. *CrystEngComm* **2016**, *18*, 8823–8828. [CrossRef]

42. Huang, F.; Zhang, H.; Banfield, J.F. Two-stage crystal-growth kinetics observed during hydrothermal coarsening of nanocrystalline ZnS. *Nano Lett.* **2003**, *3*, 373–378. [CrossRef]

43. Matthews, A. The crystallization of anatase and rutile from amorphous titanium dioxide under hydrothermal conditions. *Am. Mineral.* **1976**, *61*, 419–424.

44. Penn, R.L.; Banfield, J.F. Morphology development and crystal growth in nanocrystalline aggregates under hydrothermal conditions: Insights from titania. *Geochim. Cosmochim. Acta* **1999**, *63*, 1549–1557. [CrossRef]

45. Voorhees, P.W. The theory of Ostwald ripening. *J. Stat. Phys.* **1985**, *38*, 231–252. [CrossRef]

46. Byrappa, K. Hydrothermal growth of polyscale crystals. In *Springer Handbook of Crystal Growth*; Springer: Berlin/Heidelberg, Germany, 2010; pp. 599–653.

47. Murowchick, J.B.; Barnes, H. Effects of temperature and degree of supersaturation on pyrite morphology. *Am. Mineral.* **1987**, *72*, 1241–1250.

48. Xiong, Y.; Wood, S.A. Experimental quantification of hydrothermal solubility of platinum-group elements with special reference to porphyry copper environments. *Miner. Petrol.* **2000**, *68*, 1–28. [CrossRef]

49. Liu, K.; Gao, X.L.; Li, L. Advances in trace platinum group elements speciation and preconcentration of chelate resins in seawater. *Chin. J. Appl. Ecol.* **2017**, *28*, 3424–3432.

50. Chang, H.; Chu, X. Pyrite Framboids and Palaeo ocean Redox Condition Reconstruction. *Adv. Earth Sci.* **2011**, *26*, 475–481.

51. Gao, B.; Nakano, S.; Kakimoto, K. The impact of pressure and temperature on growth rate and layer uniformity in the sublimation growth of A1N crystals. *J. Cryst. Growth* **2012**, *338*, 69–74. [CrossRef]

52. Resing, J.A.; Sedwick, P.N.; German, C.R.; Jenkins, W.J.; Moffett, J.W.; Sohst, B.M.; Tagliabue, A. Basin-scale transport of hydrothermal dissolved metals across the South Pacific Ocean. *Nature* **2015**, *523*, 200–203. [CrossRef]

53. Zeng, Z.G.; Zhang, Y.X.; Chen, Z.X.; Ma, Y.; Wang, X.Y.; Zhang, D.D. Geological Tectonics, Magmatism and Seafloor Hydrothermal Activity in the Back-Arc Basins of the Western Pacific. *Studia Mar. Sin.* **2016**, *51*, 3–36. (In Chinese with English abstract)